

Journal of Materials Chemistry A

Accepted Manuscript



This is an *Accepted Manuscript*, which has been through the Royal Society of Chemistry peer review process and has been accepted for publication.

Accepted Manuscripts are published online shortly after acceptance, before technical editing, formatting and proof reading. Using this free service, authors can make their results available to the community, in citable form, before we publish the edited article. We will replace this *Accepted Manuscript* with the edited and formatted *Advance Article* as soon as it is available.

You can find more information about *Accepted Manuscripts* in the [Information for Authors](#).

Please note that technical editing may introduce minor changes to the text and/or graphics, which may alter content. The journal's standard [Terms & Conditions](#) and the [Ethical guidelines](#) still apply. In no event shall the Royal Society of Chemistry be held responsible for any errors or omissions in this *Accepted Manuscript* or any consequences arising from the use of any information it contains.



COMMUNICATION

Three dimensional architecture of Carbon Wrapped Multilayer $\text{Na}_3\text{V}_2\text{O}_2(\text{PO}_4)_2\text{F}$ Nanocubes Embedded in Graphene for improved sodium ion batteries

Received 00th January 20xx,
Accepted 00th January 20xx

DOI: 10.1039/x0xx00000x

www.rsc.org/

Hongyun Jin,^{ab} Jie Dong,^a Evan Uchaker,^b Qifeng Zhang,^b Xueze Zhou,^b Shuen Hou,^a Jiangyu Li,^c and Guozhong Cao^{b*}

A novel $\text{Na}_3\text{V}_2\text{O}_2(\text{PO}_4)_2\text{F}$ @Carbon/Graphene three dimensional (3D) architecture (NVPF@C/G) is developed through a simple approach for the first time. It exhibits greatly improved rate capability and delivers a reversible capacity of 113.2 mAhg⁻¹ at 1C.

Introduction

With major concerns regarding energy storage and conversion issues, lithium ion batteries (LIBs) have played a dominant role and occupied the majority share of the rechargeable battery sector.¹⁻⁵ Wide-scale application of LIBs correlates to huge demand for lithium resource; consequently the cost of Li compounds has tripled in the past five years alone. At the meantime, sodium ion batteries (SIBs) emerge recently and have attracted increasing attention. Sodium holds promise for being a natural complement that can potentially even serve as substitute for LIBs due to its high similarity in chemical properties with Li.⁶⁻⁹ Most importantly, elemental sodium is distributed nearly everywhere throughout the world, and its abundance 2.64%, is nearly 440 times greater than that of Li. Moreover, sodium does not react with aluminum foil, meaning that copper can be replaced with cheaper aluminum as the current collector in SIBs.^{10, 11} Therefore, SIBs have drawn considerable attention in recent years in view of their low cost compared to LIBs.¹²⁻¹⁶ A great range of sodium-based compounds are being investigated as possible electrode materials for SIBs, such as $\text{Na}_3\text{V}_2(\text{PO}_4)_3$,¹⁷⁻²¹ $\text{Na}_3\text{V}_2(\text{PO}_4)_2\text{F}_3$,^{22, 23} NaMO_2 (where M = V, Ni, Mn, Cr, Al, Co),²⁴ NaFePO_4 ,²⁵ $\text{Na}_2(\text{Fe, Mn})\text{PO}_4\text{F}$,²⁶ NaVPO_4F ,²⁷ $\text{Na}_3\text{V}_2\text{O}_{2x}(\text{PO}_4)_2\text{F}_{3-2x}$,²⁸⁻³¹ $\text{Na}_3\text{V}_2\text{O}_2(\text{PO}_4)_2\text{F}$,³²⁻³⁴ etc. Among these compounds, $\text{Na}_3\text{V}_2\text{O}_2(\text{PO}_4)_2\text{F}$ (NVPF) has attracted a great deal of attention because it has two high-voltage plateaus at approximately 3.65 and

4.1 V vs. Na/Na^+ , and a relatively large intercalation capacity (130 mAhg⁻¹) as two Na^+ can be inserted and extracted during the dis/charge process. Rojo's group reported a mixed-valence sodium vanadium fluorophosphates SIB material with general formula $\text{Na}_3\text{V}_2\text{O}_{2x}(\text{PO}_4)_2\text{F}_{3-2x}$ synthesized by hydrothermal method that displayed 80 mAhg⁻¹ at 1C with no capacity fading after 30 cycles.^{30, 31} The same group went on to synthesize $\text{Na}_3(\text{VO})_2(\text{PO}_4)_2\text{F}$ by ex-situ carbon coating, which delivered a capacity of 68 mAhg⁻¹ at 1C.³² However, because the electronic conductivity of common carbon materials is not sufficiently high, the high-rate discharge capability remains unsatisfactory. Graphene, with an electron mobility value higher than $1.5 \times 10^4 \text{cm}^2 \text{V}^{-1} \text{s}^{-1}$ at room temperature has been utilized in LIB and SIB electrode materials.^{35, 36} Recently, Goodenough et al. reported a $\text{Na}_3\text{V}_2\text{O}_2(\text{PO}_4)_2\text{F}$ /Graphene sandwich nanostructure prepared by a solvothermal method that delivers a discharge capacity around 100.4 mAhg⁻¹ at 1C, meanwhile, they confirmed the presence of the two voltage plateaus at 3.65 and 4.05V by first-principle calculations.^{33, 34} For high power application, electrode materials for SIB must possess rapid electron transport and ion diffusion capability.^{37, 38} Carbon coating is a propitious solution to meet this requirement, and hence various kinds of carbon (graphene, matrix, carbon tube, fiber, particle, etc), have been employed as core-shell or sandwich structures in order to improve the conductivity of the electrode materials.³⁹⁻⁴³ However, the conductivity of carbon in core-shell structures is typically not high enough, thus precipitating the need for thick shelled carbon coating, but thicker carbon coating impedes sodium ion diffusion and worsens conductivity; the poor electronic conductivity or ionic diffusion of the electrode material would yield unsatisfying rate performance and cycle stability when used in SIB.^{30, 41} The sandwich structure solves the poor conductivity obstacle in the core-shell structure to some extent. Most noticeably, the conductivity of the particles wrapped by graphene located at the top and bottom of the structure is improved, but it is difficult to get a monolayer of particles between graphene layers, while multilayer particle structures are more commonplace. In a multilayer particle structure, the conductivity of the particles located in the middle of the layer, and thus not in contact with the graphene, is extremely poor and is a crucial issue. An electrode architecture consisting of

^a Address here. Faculty of Materials Science & Chemistry, China University of Geosciences, Wuhan, 430074, China.

^b Department of Materials Science & Engineering, University of Washington, Seattle, WA, 98195, USA.

^c Department of Mechanical Engineering, University of Washington, Seattle, WA, 98195, USA.

† Electronic Supplementary Information (ESI) available: [details of any supplementary information available should be included here]. See DOI: 10.1039/x0xx00000x

regular 3D highly-conductive structure with nano-scale electro-active particles has been proven to provide more efficient ion and electron transport capability.⁴³⁻⁴⁶ Nevertheless, to our best knowledge, there has been no report on the 3D architecture of NVPF@C/G.

To compensate for these deficiencies, we propose to use NVPF nanocubes embedded in graphene sheets, and wrapped with carbon to fabricate a core-shell structure; thus, NVPF particles are networked by carbon and tethered to graphene to forge a large open and highly-conductive network that can facilitate both sodium ion and electron transport. In this study, for the first time, we designed a novel NVPF@C/G 3D architecture by a combination of hydrothermal method paired with carbon deposition. The resulting NVPF@C/G was evaluated as a cathode material for SIB and presented a high reversible capacity of 137.5 mAh g⁻¹ at 0.05 C with a comparable initial coulombic efficiency of 100.9%; moreover, the material exhibited greatly improved rate capability (113.2 mAh g⁻¹ at 1 C) and 98.9% capacity retention over 40 cycles at 1 C.

Experimental section

Synthesis: The synthesis process of NVPF@C/G takes place in two steps. First, NVPF/Graphene (NVPF/G) composite material was prepared by hydrothermal method. Graphene oxide, prepared by a modified Hummers method, was immersed 50 mL N,N-dimethyl formamide (DMF) and ultrasonically treated for 24 hours. In a typical synthesis, 2 mmol NH₄H₂PO₄ (Sigma-Aldrich, 99.9% purity), 2 mmol NH₄VO₃ (Sigma-Aldrich, 99.99% purity), 1 mmol NaF (Sigma-Aldrich, 99% purity) and 1 mmol Na₂CO₃ (Sigma-Aldrich, 99.9% purity) were separately dissolved in 5 mL distilled water. The four precursor solutions were then added to the NVPF/G-DMF solution, and stirred for 30 minutes at 90 °C. Then, the mixture was sealed in a 100 mL capacity polytetrafluoroethylene (PTFE) lined stainless steel autoclave, which was maintained at 180 °C for 24 hours, and then naturally cooled to room temperature. A brown product was obtained after washing repeatedly with distilled water and ethanol. Secondly, 50 mg of the resulting powder was dissolved in distilled water and stirred for 30 min, then 12 mg sucrose was added into the suspension under vigorous stirring and heating at 105 °C until dried. The powder mixture was ground and annealed at 550 °C for 1 h in flowing argon atmosphere.

Characterization: The phase of NVPF@C/G sample were characterized by X-ray diffraction (XRD, D8 Bruker X-ray diffractometer) with Cu-K_α radiation within the range of 10° to 70° (2θ), a step size of 0.02°, and an exposure time of 10 s. The accelerating voltage and current were 40 kV and 40 mA. X-ray photoelectron spectroscopy was completed using a Surface Science Instruments S-probe spectrometer (XPS, The rmo ESCALAB 250XI) with Al K_α (hν=1486.6 eV) as the X-ray source. The X-ray spot size was 800 μm and the take-off angle was 55°, corresponding to a sampling depth of approximately 50 Å. XPS data analysis was carried out using the Service Physics ESCA 2000-A analysis program (Service Physics, Bend, OR). Microscopy investigations were performed using a JEOL JSM-7000F Scanning Electron Microscopy (SEM) and FEI Tecnai G20 Transmission Electron Microscopy (TEM) operating at 200 kV. The compositional analysis on the as-prepared samples was analyzed with Thermogravimetric Analysis system (TGA), an accessory of SEM.

Electrochemical analysis: For electrochemical analysis, 2016 type half-cells were assembled in a glove box (Mbraun) filled with high

purity argon. The cathode slurry was prepared by dispersing the as-prepared sample, Super P conductive carbon (Timcal), and PVDF binder in a NMP solvent at a respective weight ratio of 75:20:5. The slurry was then spread onto aluminum foil current collector and dried in a vacuum oven at 80 °C overnight. Sodium metal (Sigma Aldrich), 1 M NaClO₄ in ethylene carbonate (EC)/dimethyl carbonate (DMC) (1:1 v/v), and a glass fiber were used as the counter/reference electrode, electrolyte, and separator for the Na-ion half-cells, respectively. Cyclic voltammetry (CV) was completed using an electrochemical analyzer (CH Instruments, Model 605C) in the voltage range of 4.3-2.0 V (vs. Na/Na⁺) at scanning rates ranging from 0.1 to 0.8 mV s⁻¹. The current density and cycle stability performance of the sample were evaluated using the Arbin Battery Tester (BT-2000, Arbin Instruments) operating at room temperature. The half-cells were tested within the voltage range of between 2.0V to 4.3V vs. Na/Na⁺ at various charging rates, and assuming 1 C current density of 130 mA g⁻¹; capacity values were normalized to the mass of NVPF@C/G alone.

Results and discussion

The detailed assembly process and formation mechanism of the NVPF@C/G 3D architecture is illustrated in Figure 1. Ultrasonically treated graphene oxide was combined with several precursor solutions as to insert F⁻, Na⁺, PO₄³⁻ and VO₃⁻ ions into the graphene interlayer. Then, V⁵⁺ and graphene oxide were reduced by DMF in a hydrothermal process. Along with graphene oxide reduction, NVPF was ensuingly nucleated and entrenched onto the graphene sheets. As the reaction time progressed, NVPF crystallized and grew, while the graphene layers were exfoliated to single or few layered sheets. Subsequently, NVPF crystals developed a cubic morphology, and then self-assembled into a structure of multilayer of NVPF particles as shown in Figure 1(c). The as-prepared NVPF/Graphene composite was immersed in a sucrose solution, then dried and annealed in argon. As a result, carbon nanoparticles homogeneously wrap the NVPF nanocubes and complete fabrication of the core-shell while maintaining connection to the graphene. Consequently, the carbon wrapped multilayer Na₃V₂O₂(PO₄)₂F nanocubes pillared graphene 3D architecture was obtained.

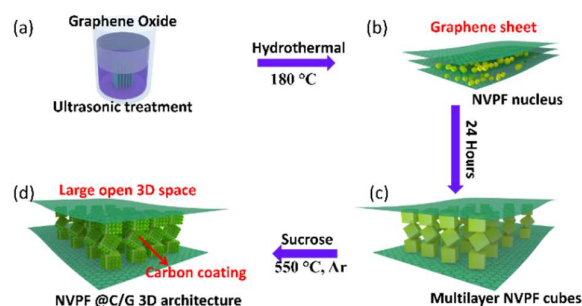


Figure 1. Schematic illustration of the assembly process and formation mechanism of the NVPF@C/G 3D architecture

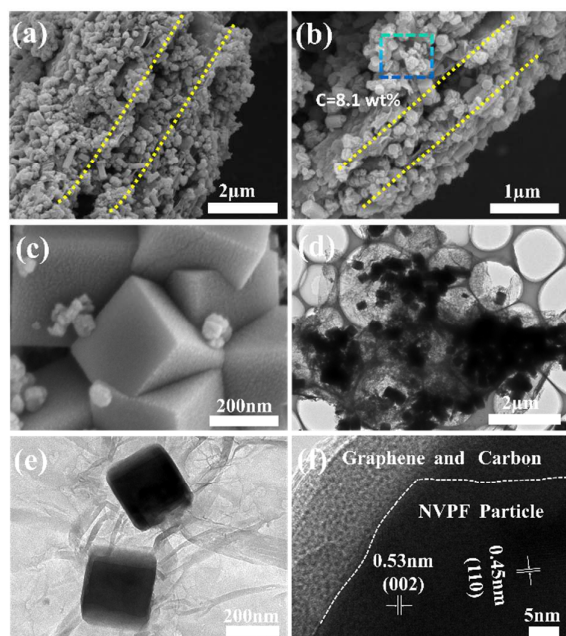


Figure 2. SEM and TEM images of NVPF@C/G specimen prepared by hydrothermal method: (a-b) Overall views of NVPF@C/G displaying a typical layered structure; (c) Representative view of multilayered NVPF@C/G cubes between graphene layers; (d-f) TEM and HRTEM images of NVPF@C/G.

The morphology and structural characteristics of the NVPF@C/G were examined by scanning (SEM) and transmission (TEM) electron microscopy. Figure 2 (a, b) reveals that the NVPF@C/G possess a layered structure, as shown from various perspectives. Multiple layers of NVPF cubes stack between the parallel graphene sheets, which are featured by the dashed yellow lines, and the assembly of three or more layers of particles was clearly seen (Figure 2 a, b). TGA was conducted in order to analyze the region in Figure 2 (b), and the carbon content in the sample was approximately 8.1 wt% (Figure S1). In addition, the micrographs suggest that the reduced graphene was exfoliated to sheets during the hydrothermal process, after which the NVPF nanocubes were anchored on the graphene sheets as shown in Figure 2 (a, b). The high-magnification SEM micrograph clearly depicts the multilayered particle structure interlaminated between graphene layers, in which the NVPF nanocubes stack in an edge-face sharing manner (Figure 2 c). TEM images in Figure 2 (e, f) show that the carbon nanoparticle coating is uniformly distributed on the surface of the NVPF nanocubes, effectively forming a core-shell structure. The TEM image in Figure 2 (d) unveils that many NVPF nanocubes stack together between the graphene layers, corroborating the multilayer structure observed in SEM (Figure 2 (a, b)). The observed lattice spacing values are 0.53 nm and 0.45 nm, corresponding to (002) and (110) facet, respectively, which is in accordance with the XRD results (Figure 2 (f), Figure S2). The NVPF nanocubes have an approximate edge length of 200 nm; such small particle size signifies shorter transporting lengths for both electrons and ions, resulting in fast charge-discharge transfer kinetics. Furthermore, carbon was observed on the edge side of the NVPF nanocubes in Figure 2 (e). Similar results arising from the high resolution images in Figure 2 (f) indicate that the cube surface

was wrapped with graphene and carbon. In this instance, graphene can be described as an “express way” and the carbon as “interstates” that comprise an overall network, where electrons can travel freely and ultrafast and hence improve the cycle capability and rate performance.

The powder X-ray diffraction pattern (XRD) of NVPF@C/G is shown in Figure 3 (a). All the diffraction patterns are well in agreement with the standard pattern for tetragonal $\text{Na}_3\text{V}_2\text{O}_2(\text{PO}_4)_2\text{F}$ (PDF 76-3645), space group $I4/mmm[139]$ with the lattice parameters $a=b=6.370 \text{ \AA}$ and $c=10.637 \text{ \AA}$, which is well match with that in literature.³³ In this XRD pattern, there is a weak diffraction peak around $2\theta \approx 23^\circ$ that corresponds to the reduced graphene phase according to the literature and compared to the Figure S3.⁴⁷ No characteristic carbon peaks are detected, which indicates that carbon derived from sucrose may be amorphous or the amount of crystalline carbon is below the detectable limit. The layer structure of NVPF, as displayed in Figure 3 (b), provides preferential pathways for the Na^+ to transport in this host.^{33, 48, 49} This framework structure is formed by layers of $[\text{VO}_5\text{F}]$ octahedral and $[\text{PO}_4]$ tetrahedral units. Between these layers, pairs of $[\text{VO}_5\text{F}]$ octahedra and $[\text{PO}_4]$ tetrahedral are connected by shared oxygen atoms as exhibited in the lower-left corner, while the $[\text{VO}_5\text{F}]$ octahedra are bridged by a fluorine atom between layers as shown in the lower-right corner. Between different layers, there is a broad channel for the transportation of sodium ions. This open framework structure is beneficial for sodium ion intercalation and rapid diffusion during the battery charge and discharge processes. X-Ray photoelectron spectroscopy (XPS) was then conducted to gather information on the chemical nature of the sample. The high-resolution C1s spectra depicts C=C (sp^2) and C-C (sp^3) peaks at 284.8 and 285.5 eV, respectively. Additionally, small peaks corresponding to C-O and C=O separately located at 286.5 and 288.4 eV, respectively, suggests the graphene oxide was nearly completely reduced. The high-resolution V2p_{3/2} and V2p_{1/2} XPS spectra reveal the characteristic main and satellite peaks with a binding energy of 516.4 and 523.4 eV, respectively. The peak locations and lack of shoulder verifies the valence of vanadium in the sample as +4, which matches well with the literature values and is consistent with the XRD results.^{50, 51}

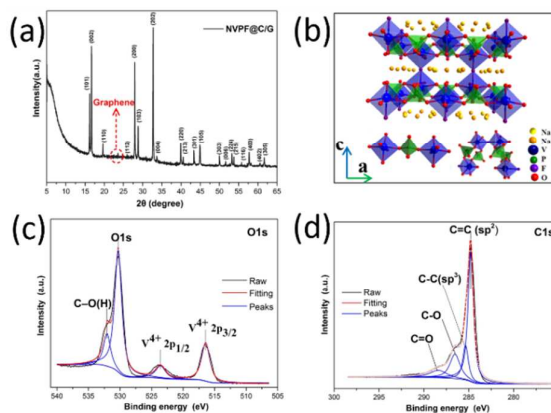
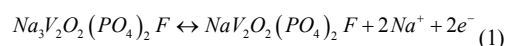


Figure 3. (a) XRD patterns of NVPF@C/G; (b) Schematic representation of the NVPF crystal structure; (c) High-resolution O1s and V2p XPS spectra of NVPF@C/G; (d) High-resolution C1s XPS spectra of NVPF@C/G.

To further evaluate the electrochemical behavior of the NVPF@C/G electrode material, cyclic voltammetry (CV) and galvanostatic charge-discharge cycling are carried out. Figure 4 (a) depicts the CV curves of NVPF@C/G at a scan rate 0.5 mVs⁻¹ over the potential range of 2-4.3 V vs. Na/Na⁺, in which a pair of reversible redox peaks, corresponding to the insertion and extraction of sodium ions into/out the host NVPF, were displayed. The sharp peaks and symmetrical feature of the CV curves validate the reversibility of the system. To the best knowledge of the authors, this is the first time the CV curves of NVPF@C/G are reported, although there is polarization phenomena.^{30, 33} In the first cycle, two anodic peaks located at 3.75 and 4.18 V vs. Na/Na⁺ correspond to the release of sodium ions as the mechanism described in Equation (1). Conversely, two cathodic peaks located at 3.48 and 3.88 V vs. Na⁺/Na are related to the insertion of sodium ions to NVPF, resulting in the formation of V⁴⁺ as described in Equation (2).²⁸

Desodiation:



Sodiation:

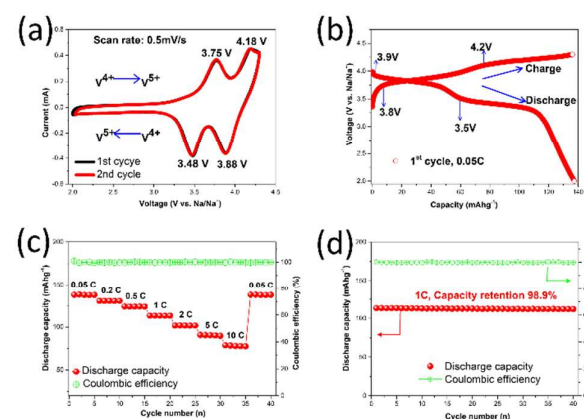
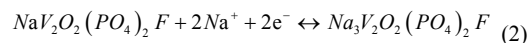


Figure 4. Electrochemical properties of the NVPF@C/G when tested as SIB cathode material: (a) 1st and 2nd CV curves at a scan rate of 0.5 mVs⁻¹; (b) Initial charge-discharge voltage profiles at 0.05C; (c) rate capability; (d) cycle stability at 1C up to 40 cycles.

Moreover, the redox peak position and shape of the 2nd CV curve exactly overlaps with the first, implying excellent electrochemical reversibility. This reversibility can be attributed to NVPF nanocubes wrapped by carbon and embedded in graphene sheet, which keep the NVPF structure stable during the sodium ion intercalation/deintercalation reactions.^{21, 52}

Figure 4 (b) presents the initial charge and discharge curves of a NVPF@C/G half-cell at 0.05C. Two potential plateaus in the charge process were clearly observed, one plateau at approximately 3.8V and another at 4.2V; the discharge plateaus (around 3.9 and 3.5V) suggest that the discharge curve corresponds well with the anodic peaks seen in the CV curves. In the initial charge/discharge cycle at 0.05C, as shown in Figure 4 (b), the battery can deliver a discharge capacity of 137.5 mAhg⁻¹ and homologous charge capacity of 136.2 mAhg⁻¹, in accordance with a coulombic efficiency of 100.9%

indicating excellent reversibility. Such a high first cycle efficiency is infrequent for NVPF SIB electrodes, as compared to Goodenough's and Rojo's first efficiencies of <94% and <95%, respectively, which is likely due to the partial irreversible insertion of sodium ions into the channel of the NVPF in the first discharge cycle; part of the sodium ions remain in the NVPF and fail to get out during the next charge cycle^{30, 33}. From Figure 4 (c), the specific discharge capacities tested in the voltage window from 2.0 to 4.3 V are 137.5, 130.4, 123.9, 113.2, 101.7, 90.7 and 78.5 mAhg⁻¹ at 0.05 C, 0.2 C, 0.5C, 1C, 2C, 5C and 10C, respectively. With increasing the charge and discharge current densities, the material only shows a moderate decrease in the capacity between discharge rates; such characteristics indicate excellent rate performance, and confirms that NVPF@C/G is suitable for sodium ion insertion/extraction at higher rates. Moreover, the present discharge capacity values are some of the best compared to previously reported results, particularly at high rate. This performance is possibly due to the large open structure and the high-conductivity network that enhances electron transport capability and hence improves sodium ion storage capacity and storage kinetics.^{53, 54}

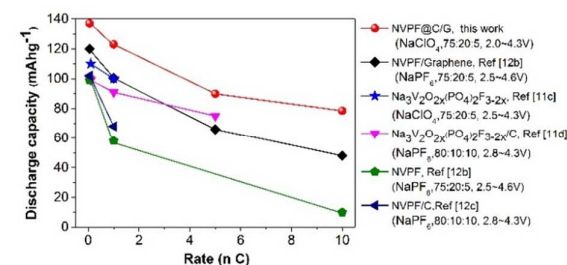


Figure 5. Comparison of rate performance of this work with other NVPF-based electrode materials in SIBs reported recently. (The plot shows the discharge capacities according to the total mass of electrode materials; the legend contains the ratio of active materials: carbon: binder and the voltage window against Na/Na⁺)

Figure 4 (d) shows the cycle performance at 1C, where the initial discharge capacity is 113.4mAhg⁻¹ that only drops to 112.1mAhg⁻¹ after 40 cycles; the capacity retention is thus 98.9%. Furthermore, the coulombic efficiency is close to 100% (the minimum coulombic efficiencies is 99.4%) throughout cycling, suggesting a superior electrochemical reversibility and cycle stability. This capacity retention can mainly be attributed to the carbon core-shell structure and the NVPF cubes tethered to graphene, which preserves the NVPF structure from collapsing during the sodium ion insertion and extraction processes.^{17, 41} Many other reports have also announced that graphene addition, carbon coating and other coating can improve the battery cyclic stability.^{20, 39} We also compared our work with previous NVPF-based electrode materials tested for SIBs, including Na₃V₂O₂(PO₄)₂F_{3-2x}, Na₃V₂O₂(PO₄)₂F_{3-2x}-C composite, Na₃V₂O₂(PO₄)₂F and Na₃V₂O₂(PO₄)₂F/graphene, and summarized the results in Figure 5; however, it should be noted that the electrolyte, quantity of conductive carbon or binder, and voltage window may have varied some in these other studies. Unequivocally, the material synthesized in this study displayed superior electrochemical behavior. The high capacity, good rate performance, cycle stability and excellent reversibility of

NVPF@C/G can be mainly ascribed to the following: (1) The nano-scale NVPF cubes shortened both the electron and ion transport distance; (2) Owing to NVPF tethered to the graphene sheets, the electrolyte and sodium ion diffusion are enhanced by the relatively fixed open interspaces; (3) The high-conductivity network consisting of a graphene “express way” and carbon “interstates” efficiently accelerates electron transport, thereby enabling the electrons to travel anywhere within the NVPF nanocubes ultrafast during the redox reaction. Another possible reason leading to the performance enhancement maybe arises from the carbon core-shell and cubes tethered to graphene sheet, which can prevent the NVPF structural change to some degree during the sodium-ion insertion/desertion process. However, this needs to be confirmed in future by a further study based on in-situ HR-TEM characterization.

Conclusion

In summary, we have presented a new approach to fabricate an innovative 3D architecture-NVPF@C/G, with carbon wrapped multilayer $\text{Na}_3\text{V}_2\text{O}_5(\text{PO}_4)_2\text{F}$ nanocubes embedded in graphene structure for the first time. When the as-obtained NVPF@C/G, was used as a cathode material for SIB, it exhibited high initial reversible capacity of 113.2 mAhg^{-1} at 1C, which is the champion value to date. In addition, the capacity maintains at 112.1 mAhg^{-1} after 40 cycles at 1C, and the discharge capacity retention is 98.9%. Furthermore, the CV curves of NVPF@C/G were reported for the first time. The idea of using NVPF nanocubes wrapped by carbon embedded in graphene sheets configuration may be successfully implemented for other sodium and lithium ion battery electrode materials as a way to further improve conductivity or potentially even other layered composite materials used in advanced electro-optic fields.

Acknowledgements

Part of this work was financially supported in part by the National Science Foundation (NSF, CMMI-1030048), National Nature Science Foundation of China (NSFC51102218), Natural Science Foundation of Hubei Province (No:2013CFB412), China University of Geosciences (Wuhan) (CUG120402, CUG120118) and the University of Washington TGIF grant.

Notes and References

1. M. Armand and J. M. Tarascon, *Nature*, 2008, **451**, 652-657.
2. J. Lee, A. Urban, X. Li, D. Su, G. Hautier and G. Ceder, *Science*, 2014, **343**, 519-522.
3. Z. W. Seh, W. Li, J. J. Cha, G. Zheng, Y. Yang, M. T. McDowell, P.-C. Hsu and Y. Cui, *Nature Communications*, 2013, **4**.
4. L. Shen, E. Uchaker, X. Zhang and G. Cao, *Advanced Materials*, 2012, **24**, 6502-6506.
5. X. Li, M. Gu, S. Hu, R. Kennard, P. Yan, X. Chen, C. Wang, M. J. Sailor, J.-G. Zhang and J. Liu, *Nature communications*, 2014, **5**.
6. C. Cao, W. Liu, L. Tan, X. Liao and L. Li, *Chemical Communications*, 2013, **49**, 11740-11742.
7. S. W. Kim, D. H. Seo, X. Ma, G. Ceder and K. Kang, *Advanced Energy Materials*, 2012, **2**, 710-721.
8. W. Luo, M. Allen, V. Raju and X. Ji, *Advanced Energy Materials*, 2014.
9. N. Yabuuchi, M. Kajiyama, J. Iwatate, H. Nishikawa, S. Hitomi, R. Okuyama, R. Usui, Y. Yamada and S. Komaba, *Nature Materials*, 2012, **11**, 512-517.
10. M. Mikkor, *Journal of the Electrochemical Society*, 1985, **132**, 991-998.
11. E. Uchaker, Y.-Z. Zheng, S. Li, S. L. Candelaria, S. Hu and G. Cao, *Journal of Materials Chemistry A*, 2014, **2**, 18208-18214.
12. X. Han, Y. Liu, Z. Jia, Y.-C. Chen, J. Wan, N. Weadock, K. J. Gaskell, T. Li and L. Hu, *Nano letters*, 2013, **14**, 139-147.
13. M. D. Slater, D. Kim, E. Lee and C. S. Johnson, *Advanced Functional Materials*, 2013, **23**, 947-958.
14. L. Wang, Y. Lu, J. Liu, M. Xu, J. Cheng, D. Zhang and J. B. Goodenough, *Angewandte Chemie International Edition*, 2013, **52**, 1964-1967.
15. Y. You, X.-L. Wu, Y.-X. Yin and Y.-G. Guo, *Energy & Environmental Science*, 2014, **7**, 1643-1647.
16. Y. Shao, J. Xiao, W. Wang, M. Engelhard, X. Chen, Z. Nie, M. Gu, L. V. Saraf, G. Exarhos and J.-G. Zhang, *Nano letters*, 2013, **13**, 3909-3914.
17. W. Duan, Z. Zhu, H. Li, Z. Hu, K. Zhang, F. Cheng and J. Chen, *Journal of Materials Chemistry A*, 2014, **2**, 8668-8675.
18. Z. Jian, W. Han, X. Lu, H. Yang, Y.-S. Hu, J. Zhou, Z. Zhou, J. Li, W. Chen, D. Chen and L. Chen, *Advanced Energy Materials*, 2013, **3**, 156-160.
19. Y. H. Jung, C. H. Lim and D. K. Kim, *Journal of Materials Chemistry A*, 2013, **1**, 11350-11354.
20. S. Li, Y. F. Dong, L. Xu, X. Xu, L. He and L. Q. Mai, *Advanced Materials*, 2014, **26**, 3545-3553.
21. K. Saravanan, C. W. Mason, A. Rudola, K. H. Wong and P. Balaya, *Advanced Energy Materials*, 2013, **3**, 444-450.
22. W. Song, Z. Wu, J. Chen, Y. Zhu, H. Hou, Q. Lan and X. Ji, *Langmuir*, 2014.
23. Y. Wang, M. Klenk, K. Page and W. Lai, *Chemistry of Materials*, 2014, **26**, 5613-5624.
24. K. Chihara, A. Kitajou, I. D. Gocheva, S. Okada and J.-i. Yamaki, *Journal of Power Sources*, 2013, **227**, 80-85.
25. V. Palomares, P. Serras, I. Villaluenga, K. B. Hueso, J. Carretero-Gonzalez and T. Rojo, *Energy & Environmental Science*, 2012, **5**, 5884-5901.
26. R. Tripathi, S. M. Wood, M. S. Islam and L. F. Nazar, *Energy & Environmental Science*, 2013, **6**, 2257-2264.
27. J. Song, M. Xu, L. Wang and J. B. Goodenough, *Chemical Communications*, 2013, **49**, 5280-5285.
28. K. B. Hueso, M. Armand and T. Rojo, *Energy & Environmental Science*, 2013, **6**, 734-749.
29. P. Serras, V. Palomares, J. Alonso, N. Sharma, J. Miguel Lopez del Amo, P. Kubiak, M. Luisa Fdez-Gubieda and T. Rojo, *Chemistry of Materials*, 2013, **25**, 4917-4925.
30. P. Serras, V. Palomares, A. Goñi, I. G. de Muro, P. Kubiak, L. Lezama and T. Rojo, *Journal of Materials Chemistry*, 2012, **22**, 22301-22308.

31. P. Serras, V. Palomares, A. Goni, P. Kubiak and T. Rojo, *Journal of Power Sources*, 2013, **241**, 56-60.
32. P. Serras, V. Palomares, P. Kubiak, L. Lezama and T. Rojo, *Electrochem. Commun.*, 2013, **34**, 344-347.
33. M. Xu, L. Wang, X. Zhao, J. Song, H. Xie, Y. Lu and J. B. Goodenough, *Physical Chemistry Chemical Physics*, 2013, **15**, 13032-13037.
34. M. Xu, P. Xiao, S. Stauffer, J. Song, G. Henkelman and J. B. Goodenough, *Chemistry of Materials*, 2014, **26**, 3089-3097.
35. L. Shen, B. Ding, P. Nie, G. Cao and X. Zhang, *Advanced Energy Materials*, 2013, **3**, 1484-1489.
36. C. Zhu, K. Song, P. A. van Aken, J. Maier and Y. Yu, *Nano Letters*, 2014, **14**, 2175-2180.
37. J. Xie, X. Yang, S. Zhou and D. Wang, *ACS nano*, 2011, **5**, 9225-9231.
38. S. Zhou, X. Yang, Y. Lin, J. Xie and D. Wang, *ACS nano*, 2011, **6**, 919-924.
39. L.-H. Hu, F.-Y. Wu, C.-T. Lin, A. N. Khlobystov and L.-J. Li, *Nature Communications*, 2013, **4**.
40. Y. Kim, Y. Park, A. Choi, N.-S. Choi, J. Kim, J. Lee, J. H. Ryu, S. M. Oh and K. T. Lee, *Advanced Materials*, 2013, **25**, 3045-3049.
41. D. Su, H.-J. Ahn and G. Wang, *Chemical Communications*, 2013, **49**, 3131-3133.
42. Y. Wen, K. He, Y. Zhu, F. Han, Y. Xu, I. Matsuda, Y. Ishii, J. Cumings and C. Wang, *Nature Communications*, 2014, **5**.
43. Y. Yan, Y.-X. Yin, Y.-G. Guo and L.-J. Wan, *Advanced Energy Materials*, 2014, **4**.
44. T. S. Arthur, D. J. Bates, N. Cirigliano, D. C. Johnson, P. Malati, J. M. Mosby, E. Perre, M. T. Rawls, A. L. Prieto and B. Dunn, *MRS bulletin*, 2011, **36**, 523-531.
45. N. Cirigliano, G. Sun, D. Membreno, P. Malati, C. Kim and B. Dunn, *Energy Technology*, 2014, **2**, 362-369.
46. J. W. Long, B. Dunn, D. R. Rolison and H. S. White, *Chemical Reviews*, 2004, **104**, 4463-4492.
47. H. J. Shin, K. K. Kim, A. Benayad, S. M. Yoon, H. K. Park, I. S. Jung, M. H. Jin, H. K. Jeong, J. M. Kim and J. Y. Choi, *Advanced Functional Materials*, 2009, **19**, 1987-1992.
48. W. Massa, O. V. Yakubovich and O. V. Dimitrova, *Solid State Sciences*, 2002, **4**, 495-501.
49. H. Pan, Y.-S. Hu and L. Chen, *Energy & Environmental Science*, 2013, **6**, 2338-2360.
50. F. Gracia, F. Yubero, J. Espinós and A. González-Elipe, *Applied surface science*, 2005, **252**, 189-195.
51. E. Hryha, E. Rutqvist and L. Nyborg, *Surface and Interface Analysis*, 2012, **44**, 1022-1025.
52. L. Shen, H. Li, E. Uchaker, X. Zhang and G. Cao, *Nano Letters*, 2012, **12**, 5673-5678.
53. X.-C. Chen, W. Wei, W. Lv, F.-Y. Su, Y.-B. He, B. Li, F. Kang and Q.-H. Yang, *Chemical Communications*, 2012, **48**, 5904-5906.
54. F. Y. Su, Y. B. He, B. H. Li, X. C. Chen, C. H. You, W. Wei, W. Lv, Q. H. Yang and F. Y. Kang, *Nano Energy*, 2012, **1**, 429-439.

The table of contents entry:

The $\text{Na}_3\text{V}_2\text{O}_2(\text{PO}_4)_2\text{F}@$ Carbon/Graphene three dimensional (3D) architecture is designed for the first time, which demonstrates superior sodiation properties for Na-ion battery.

